

www.acsami.org Research Article

# Single-Atom Cobalt Catalysts Coupled with Peroxidase Biocatalysis for C-H Bond Oxidation

Maham Liaqat, Rumasha Nipuni Thiruwana Kankanamage, Hanyi Duan, Ryuichi Shimogawa, Jiyu Sun, Monia Nielsen, Ehab Shaaban, Yuanyuan Zhu, Puxian Gao, James F. Rusling,\* Anatoly I. Frenkel,\* and Jie He\*



Cite This: ACS Appl. Mater. Interfaces 2023, 15, 40343-40354



ACCESS

Metrics & More

Article Recommendations

Supporting Information

Access

Supporting Information

Access

Article Recommendations

Supporting Information

**ABSTRACT:** This paper reports a robust strategy to catalyze in situ C-H oxidation by combining cobalt (Co) single-atom catalysts (SACs) and horseradish peroxidase (HRP). Co SACs were synthesized using the complex of Co phthalocyanine with 3-propanol pyridine at the two axial positions as the Co source to tune the coordination environment of Co by the stepwise removal of axial pyridine moieties under thermal annealing. These structural features of Co sites, as confirmed by infrared and X-ray absorption spectroscopy, were strongly correlated to their reactivity. All Co catalysts synthesized below 300 °C were inactive due to the full coordination of Co sites in octahedral geometry. Increasing the calcination temperature led to an improvement in catalytic activity for reducing  $O_2$ , although molecular Co species with square planar coordination obtained below 600 °C were less selective to reduce  $O_2$  to  $H_2O_2$  through the two-electron pathway. Co SACs obtained at 800 °C showed superior activity in producing  $H_2O_2$  with a selectivity of 82–85% in a broad potential range. In situ production of  $H_2O_2$  was further coupled with HRP to drive the selective C-H bond oxidation in 2-naphthol. Our strategy provides new insights into the design of highly effective, stable SACs for selective C-H bond activation when coupled with natural enzymes.

**KEYWORDS:** single-atom catalysts, biocatalysis, Co phthalocyanine, horseradish peroxidase, oxygen reduction reaction (ORR), synthesis of hydrogen peroxide, C–H bond activation

# 1. INTRODUCTION

Hydrogen peroxide  $(H_2O_2)$  is of great importance for chemical syntheses, paper industries (pulp bleaching), and intercellular signaling in physiological processes. <sup>1–3</sup> As a strong oxidant,  $H_2O_2$  has been used in many oxidative synthetic reactions, e.g., epoxidation and hydroxylation. <sup>4</sup> In nature,  $H_2O_2$  can be produced in animals including humans as byproducts from the

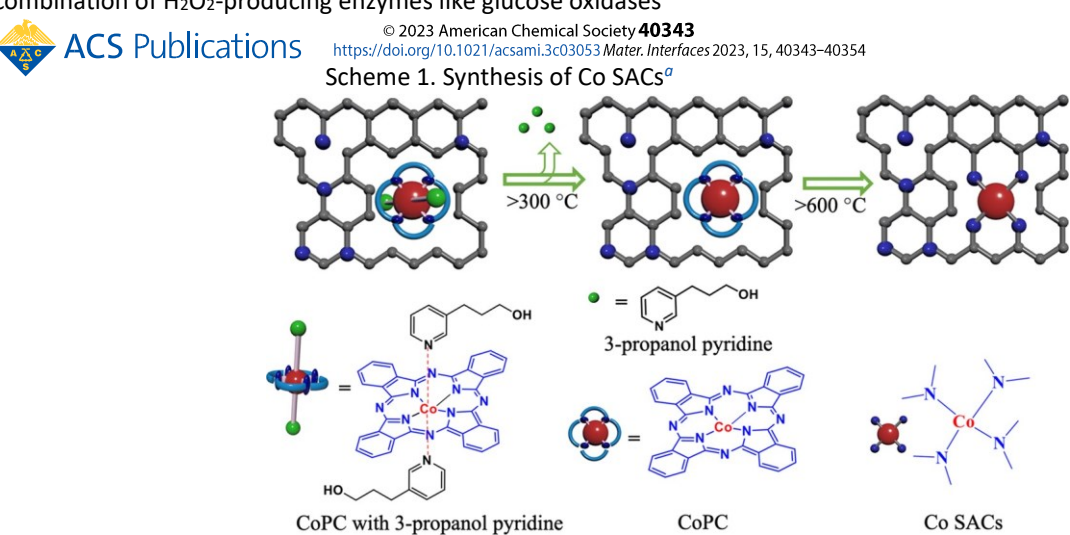
and  $H_2O_2$ -consumption enzymes like peroxidases can catalyze organic oxidations not relevant to their biofunctions.<sup>7-9</sup>

On an industrial scale,  $H_2O_2$  is produced through the anthraquinone process, where the redox cycle of hydroquinone and quinone reduces molecular  $O_2$  to  $H_2O_2$ . The regeneration of hydroquinone requires costly palladium (Pd) catalysts. On top of the typical time-consuming separation and recycling of anthraquinone, the long-term storage of relatively unstable

metabolism of fatty acids or in various fungi through the metabolism of glucose. A very well-known example is glucose oxidase, which produces  $H_2O_2$  and D-glucono-1,5-lactone by the oxidation of glucose.  $H_2O_2$  can activate many iron heme enzymes, including peroxidases and catalases, for biocatalytic oxidations. <sup>5-7</sup> In addition to their biological pathways, the combination of  $H_2O_2$ -producing enzymes like glucose oxidases

Received: March 2, 2023 Accepted: August 3, 2023 Published: August 17, 2023





<sup>a</sup>CoPC coordinated with 3-propanol pyridine loading on activated carbon and calcined at 400 and 800 °C under N₂ (Co atom in red).

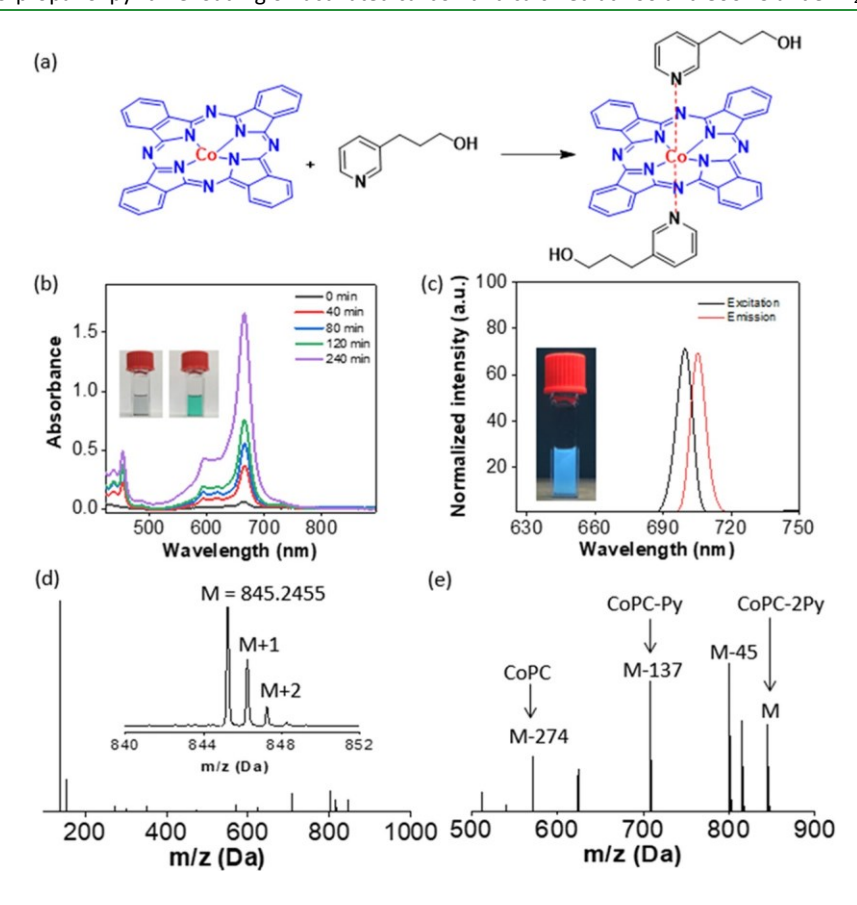


Figure 1. Synthesis of CoPC-2Py through the supramolecular interaction. (a) Coordination of CoPC with 3-propanol pyridine. (b) UV-vis spectra showing the dissolving of CoPC in the presence of 3-propanol pyridine with a molar ratio of 1:2 (mol) in chloroform, with the inset on the right showing the green color of CoPC-2Py. (c) Fluorescence spectrum of CoPC-2Py: emission (black) and excitation (red), with the inset showing the red-colored fluorescence. (d, e) MS spectra of CoPC-2Py in different m/z ranges to show the molecular ions and other fragments.

H<sub>2</sub>O<sub>2</sub> is problematic. There are a number of catalytic and noncatalytic processes to produce H2O2 in controlled quantitative yield. 10-14 For example, electrochemical synthesis of H<sub>2</sub>O<sub>2</sub> from O<sub>2</sub> is effective, controllable, and, more importantly, can be done on demand. 12 In the electrochemical reduction of O2, H2O2 can be synthesized by a two-electron transfer process:  $O_2 + 2H^+ + 2e^- \rightarrow H_2O_2$ ,  $E^\circ =$ 0.695 V vs the reversible hydrogen electrode (RHE). While an oxygen reduction reaction (ORR) on metal catalysts often involves a four-electron transfer, controlling the spatial distribution of noble metals like isolated Pd sites has shown to be very selective in reducing O2 by a two-electron transfer. 15,16 A similar perspective is demonstrated in earthabundant metalbased catalysts, e.g., molecular Cu catalysts. 13,14 It has been reported that H<sub>2</sub>O<sub>2</sub> production can be stimulated by changing the surrounding atomic structure of the metal center. 17 By finetuning the environment and the local interactions of the metal

mass, excellent stability, and low cost. 17,19-21 Heterogeneous SACs consist of metal atoms often dispersed or stabilized on a support such as conductive carbon, providing a platform for metal and surrounding environmental interactions to tune catalytic reactivity. Previous studies have suggested that nitrogen-coordinated metal sites in the form of M-N<sub>4</sub> and M-N<sub>3</sub> on nitrated carbon are very active catalysts to reduce O<sub>2</sub>.<sup>22,23</sup> These catalyst sites are structurally similar to metal atoms (or ions) surrounded by porphyrin-like ligands in hemecontaining proteins. As an example, single-atom Fe sites coordinated with N<sub>4</sub> ligands are active to reduce O<sub>2</sub> through a four-electron pathway;<sup>21,24</sup> while Co-N<sub>4</sub> is active to reduce O2 to H2O2 due to the weak interactions between Co sites with precise N-coordinated SACs for ORR. 25-29 Characterizing models of placement of SACs on support and their interaction with ligands relies on careful use of complementary methods, in which X-ray absorption spectroscopy (XAS) often plays a prominent role. 30-32.

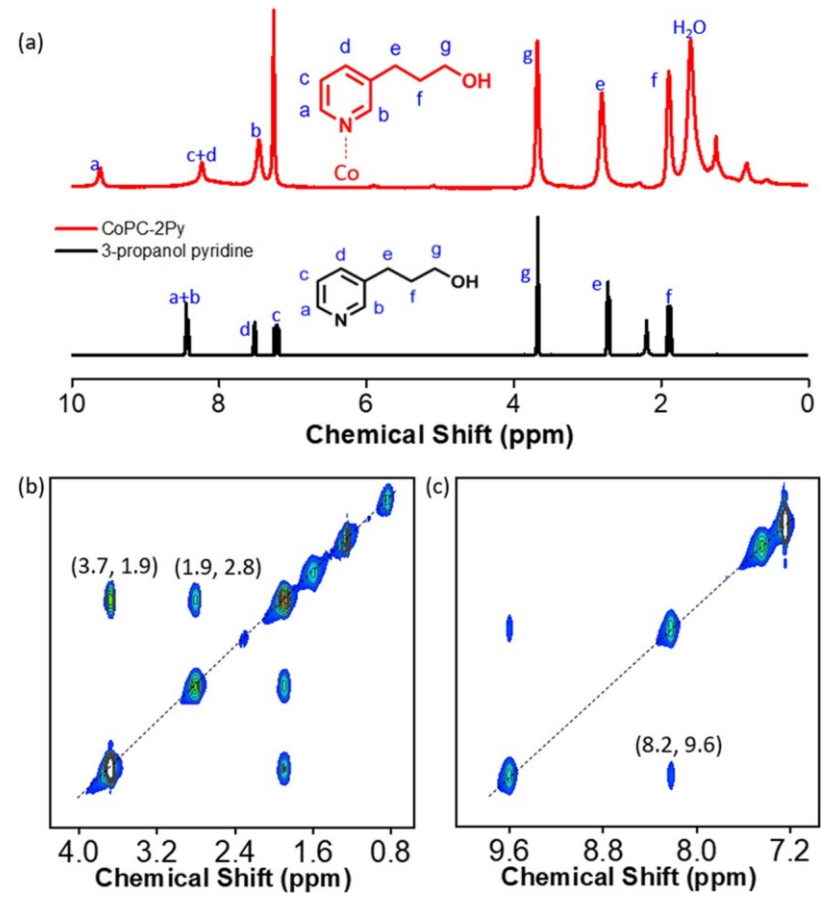


Figure 2. NMR results of the CoPC-2Py coordination complex. (a)  $^{1}$ H NMR spectra of 3-propanol pyridine (black, bottom) and CoPc-2Py (red, top) in CDCl<sub>3</sub>. (b, c)  $^{1}$ H $^{-1}$ H COSY spectrum of CoPC-2Py in CDCl<sub>3</sub> at different chemical shifts.

site, highly active early transition metal catalysts have been reported for  $H_2O_2$  production. <sup>17,18</sup>

Single-atom catalysts (SACs) have attracted a great deal of research interest due to their high catalytic activity per unit

In this paper, we report the synthesis and applications of  $Co-N_4$  SACs for  $H_2O_2$  production and its use for a cascade oxidative C-H activation catalyzed by horseradish peroxidase (HRP). The chemically stable complex cobalt

phthalocyanine (CoPC) was used to examine the impact of the coordination structure of Co sites on the activity of Co SACs. CoPC was first coordinated with 3-propanol pyridine at the two axial positions (CoPC-2Py, Scheme 1) and then loaded on activated carbon. Through annealing at high temperatures, the stepwise removal of axial pyridine moieties allowed to tune the number of N coordination of Co, as ascertained by infrared spectra and XAS analysis, and structural features were correlated with the reactivity of Co SACs. With Co SACs obtained at 800 °C, a selectivity of >80% for H<sub>2</sub>O<sub>2</sub> through two-electron reduction of O<sub>2</sub> was achieved in the potential window of -0.3 to -0.9 V vs the saturated calomel electrode (SCE, the same hereafter). In situ production of H<sub>2</sub>O<sub>2</sub> by Co SACs was used to activate HRP to catalyze the oxidative coupling of 2-naphthol to binaphthol. The combined use of Co SACs and HRP allows the controlled synthesis of H<sub>2</sub>O<sub>2</sub> and shuts down unselective radical pathways for C-C bond coupling, with a total yield of binaphthol of approximately 80% and selectivity close to 100%.

## 2. RESULTS AND DISCUSSION

We chose CoPC as the molecular Co source to make Co SACs due to their high chemical and thermal stability. Since it also has poor solubility in organic solvents,  $^{33-35}$  3-propanol pyridine was used as the axial ligand to increase its solubility. CoPC was first mixed with 3-propanol pyridine in chloroform at 1:2 (mol). The solubilization of CoPC was evidenced by the bright green solution (Figure 1b), while it was nearly colorless in the absence of 3-propanol pyridine. The dissolving of CoPC was monitored by UV–vis spectroscopy.  $^{36-39}$  A strong absorption peak at around 665 nm was assigned to the Qband ( $\pi \rightarrow \pi^*$ ) excitation arising from CoPC. The peak intensity increased with time as the concentration of bound

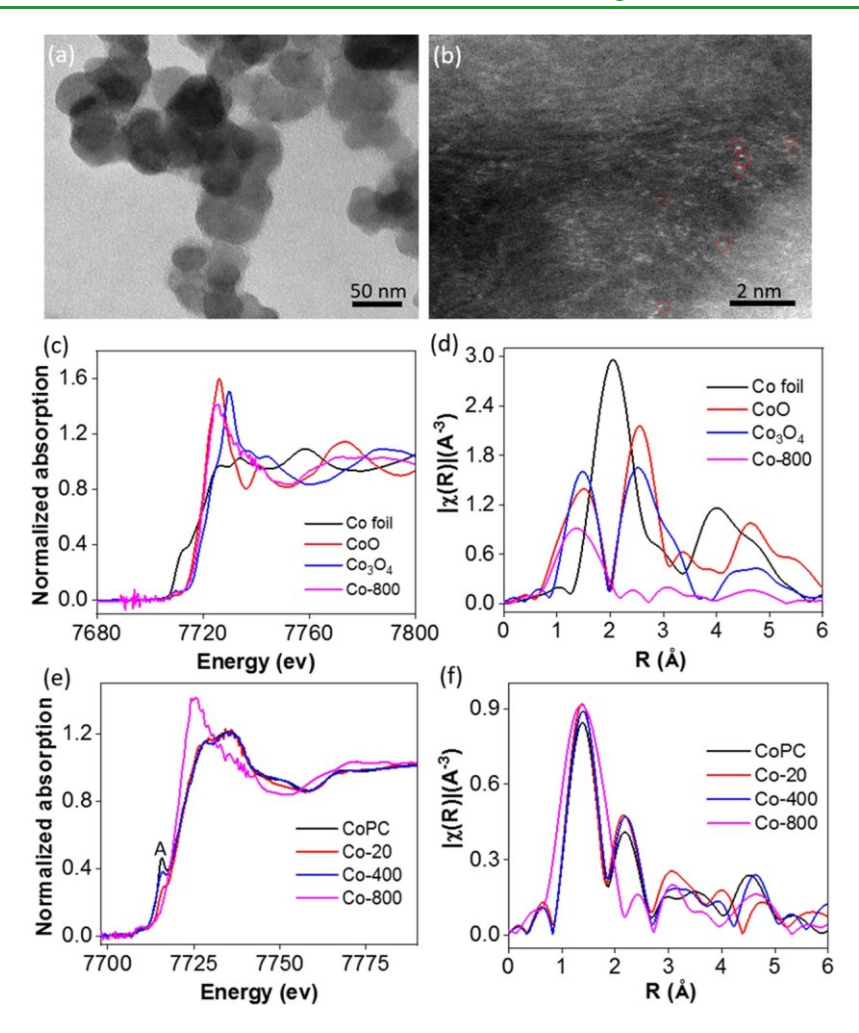


Figure 3. Morphological and coordination analysis. (a) TEM and (b) HAADF-STEM images of Co-800 supported on a carbon film. (c) XAS experiment data from the Co K-edge of the sample, reference Co metal, and Co oxides. (d) Fourier transform magnitudes of  $k^2$ -weighted EXAFS spectra collected of the sample, reference Co metal, and Co oxides. The k-range used in the Fourier transform was from 2 to 8 Å<sup>-1</sup>. (e) Normalized Co K-edge XANES spectra of Co-20 (without calcination), Co-400, Co-800, and reference samples (CoPc) and (f) Fourier transform magnitudes of  $k^2$ -weighted Co K-edge EXAFS spectra of Co-20, Co-400, Co-800, and reference samples (CoPc). The k-range used in the Fourier transform was from 2 to 8 Å<sup>-1</sup>.

CoPC increased. Without stirring, the absorbance increased to 1.6 in 4 h, corresponding to 0.017 mg/mL with the molar absorption coefficient of CoPC,  $\sim 10^5$  L·mol $^{-1}$ ·cm $^{-1}$ . $^{33}$  In chloroform, the bound CoPC complex was highly fluorescent. The maximum emission peak appeared at 706 nm (Figure 1c), very close to that of CoPC, as reported previously. $^{33,37-39}$  The dissolving was much faster under stirring, and the solubility of CoPC could reach 0.3 mg/mL after 48 h.

The formation of the CoPC complex was confirmed by <sup>1</sup>H NMR. In CDCl<sub>3</sub>, 3-propanol pyridine showed well-resolved proton peaks. After coordination with paramagnetic Co, all proton peaks were significantly broadened, where the firstorder coupling of adjacent protons disappeared (Figure 2a). The aromatic protons on the pyridine ring had an obvious shift, and the protons on the propyl alcohol far away from the coordination center were less impacted

(Supporting Information, Figure S1a). From  $^{1}H-^{1}H$ correlation spectroscopy (COSY) (Figure 2b), the protons adjacent to N (HC-N, Ha, and Hb) were largely shifted. Hb with no spin-spin interaction of neighboring protons downshifted from 8.4 to 7.4 ppm, and H<sub>a</sub> shifted from 8.4 to 9.6 ppm. The NMR results suggest that the coordination is complete without free 3-propanol pyridine, and bound 3propanol pyridine is likely under the same chemical environment. We also used mass spectroscopy to examine this complex of CoPC and 3-propanol pyridine. The complex has a molecular ion peak at m/z 845.2455, corresponding to CoPC with two 3-propanol pyridines (CoPC-2Py, C<sub>42</sub>H<sub>26</sub>N<sub>10</sub>Co, inset of Figure 1d). Therefore, the square planar Co was fully coordinated as an elongated octahedron.

Synthesis of Co SACs was done by thermal annealing. In a typical synthesis, a chloroform solution of CoPC-2Py (2 mg, 2.4  $\mu$ mol) was mixed with activated carbon (200 mg, ~50 nm nanospheres, soft-nitrided)<sup>4</sup> at a mass loading of 1 wt % of CoPC-2Py in chloroform relative to carbon. After being sonicated overnight, the solvent was slowly evaporated under N<sub>2</sub> at room temperature. The loading of CoPC-2Py was confirmed by thermogravimetric analysis (TGA), where the distinct decomposition for CoPC-2Py was around 400 °C (Figure S1). The loading amount of CoPC-2Py estimated from the weight difference was 1.2 wt %. The powder was collected and calcined at different temperatures for 2 h. We

is about 0.13 wt %, close to its initial content (see mapping analysis in Figure S4).

To further investigate the local structures of Co sites, we used XANES for Co-X catalysts calcined at different temperatures (Figure 3e). The change in Co coordination was evidenced from the pre-edge peak at 7716 eV in XANES, which is assigned to the  $1s \rightarrow 4p$  electronic transitions of Co. When the sample was treated at 400 °C, the pre-edge peak intensity had a clear decrease due to the loss of the axial pyridine moiety. The pre-edge of Co is known to decrease from octahedral to square planar coordination or, in our case, by losing the axial ligands. Linear combination

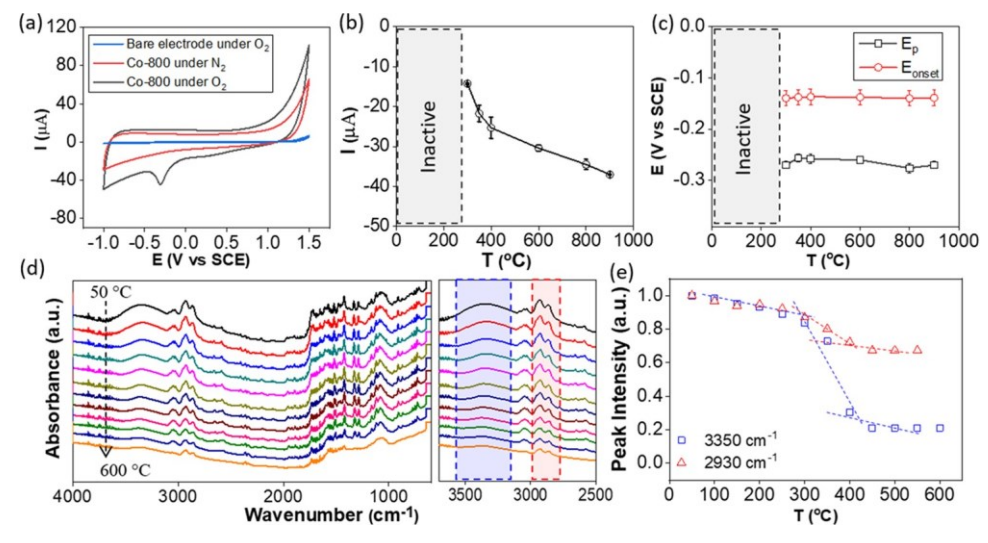


Figure 4. Catalytic activity and spectral characterization. (a, c) ORR activity of Co-800 in 0.1 M Na<sub>2</sub>SO<sub>4</sub> (pH 7). (a) CV of bare (in O<sub>2</sub> saturated) and Co-800 at 50 mV/s in N<sub>2</sub>- and O<sub>2</sub>-saturated 0.1 M Na<sub>2</sub>SO<sub>4</sub>. (b, c) Plots of peak current,  $E_{onset}$ , and  $E_{1/2}$  ( $\mu$ A) vs calcination temperatures. (d) Temperature-dependent diffuse reflectance infrared Fourier transform (DRIFT) spectra of CoPC-2Py. (e) Fourier transform infrared (FT-IR) peak intensity of the O-H and sp<sup>3</sup> C-H stretching vs temperature.

denote the samples as Co-X, where X represents the calcination temperature. Taking Co-800 calcined at 800 °C as an example, transmission electron microscopy (TEM) was first used to characterize the morphology of carbon and the dispersity of Co sites. Low-resolution TEM in Figure 3a shows the carbon nanospheres with a diameter of 50 ± 1.1 nm (Figure S2) without a morphological change after thermal annealing. Highangle annular dark-field imaging scanning TEM (HAADFSTEM) imaging provides atomic resolution of Co sites and confirms their uniform distribution on the carbon support. Under a dark field, Co sites appeared as white dots (with some representative ones encircled), indicating that Co sites are welldispersed without any agglomeration (Figure S3). Complementary Xray absorption near-edge structure (XANES) (Figure 3c) and extended X-ray absorption fine structure (EXAFS) (Figure 3d) results, together with reference Co metals and oxides, are consistent with the conclusion that Co sites in Co-800 are atomically dispersed. The final Co loading relative to carbon

analysis was conducted to estimate the fraction of the pyridine moiety. The spectrum of Co-400 was fitted to 30% of the initial sample (Co-20, as-prepared without any calcination) spectrum and 70% of CoPc, indicating that the CoPc framework with square planar coordination was retained but partial loss of the axial pyridine moiety had occurred. When the calcination temperature reached 800  $^{\circ}$ C, the pre-edge feature (1s  $\rightarrow$  4p) in the XANES spectra disappeared due to the destruction of the welldefined 4coordinated square planar structure of CoPC and the formation of atomically dispersed Co sites with lower symmetry. This structural change was also associated with a significant increase in the white line intensity of Co-800. The XANES spectrum showed nearly identical spectral features with Co SACs (as Co-N<sub>2+2</sub> supported on the defective carbon) synthesized supported on C<sub>3</sub>N<sub>4</sub> as reported previously (Figures S5 and S6).30 The EXAFS region in the kspace was too short (2-8 Å<sup>-1</sup>) for quantitative analysis by theoretical fitting. However, qualitative conclusions can be made based on Figure 3f. The fact that features in the 2-3 Å

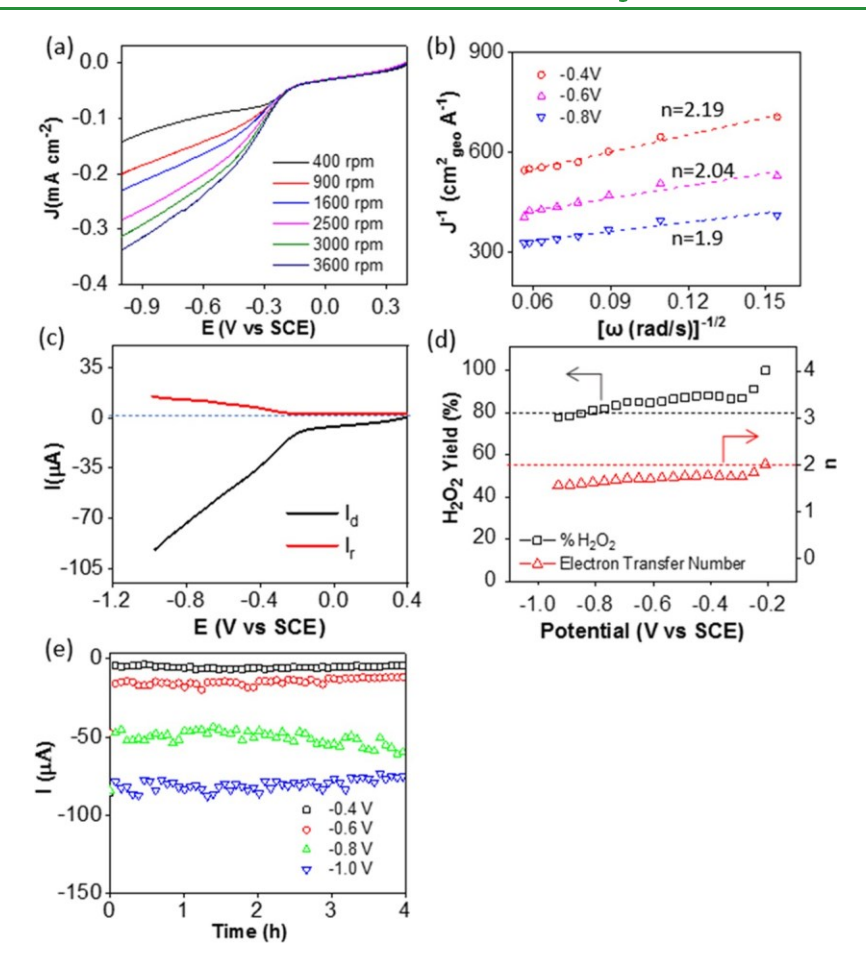


Figure 5. Electrochemical reduction of  $O_2$ . (a) RDV of Co-800 at different rotation speeds in  $O_2$  saturated 0.1 M  $Na_2SO_4$  (pH 7) at a scan rate of 50 mV/s. (b) K–L plots at different potentials and the corresponding number of electrons transferred of Co-800. (c) RRDV of Co-800 at 1600 rpms. (d) Number of electrons transferred and  $H_2O_2$  yields of Co-800 at 1600 rpms. (e) i-t curves at different potentials to investigate the stability.

range were different from those of Co metals or Co oxides (Figure 3b) is consistent with the formation of atomically dispersed Co catalysts.

The ORR activity of Co-800 was evaluated by cyclic voltammetry (CV) in 0.1 M Na<sub>2</sub>SO<sub>4</sub> saturated with O<sub>2</sub>. The working electrode was made on a pyrolytic graphite rod coated with a catalyst ink containing Co-800 and Nafion as the binder (see details in Section 4). The concentration of the Co sites was estimated to be 3.0 nmol/cm<sup>2</sup> on the electrode. Figure 4a shows typical CVs of Co-800 at a scan rate of 50 mV/s. In the N<sub>2</sub>-saturated electrolyte, no reduction peak was observed in cathodic scans. In contrast, there was an obvious peak in the O<sub>2</sub>-saturated electrolyte at -0.276 V vs SCE. As our control, the bare electrode or the pyrolytic graphite has nearly no background reduction of O<sub>2</sub>. Those results suggest that Co800 is catalytically active in reducing O<sub>2</sub>.

We examined the ORR activity of Co SACs obtained at different temperatures under the same conditions (Figure S7). There was a strong correlation between the ORR activity and the calcination temperature. First of all, the catalysts

were inactive to reduce  $O_2$  when the annealing temperature was below 250 °C, as evidenced by no reduction peak and no current increase in comparison with CVs under  $N_2$ . At 300 °C, the Co catalysts became active. The peak potential ( $E_p$ ) at the maximum reduction current is in the range of -0.27 to -0.25 V, and the onset potential ( $E_{onset}$ ), defined as the potential where the reduction current starts to increase sharply with the potential, was estimated at -0.14 V. Since  $E_p$  and  $E_{onset}$  are essentially independent of calcination temperature (Figure 4c), we assume that the active Co sites are similar in terms of their coordination geometry and environment. The current intensity ( $I_p$ ), however, increased with the thermal treatment temperature. For example, the  $I_p$  of Co-300 was  $-14.3 \pm 0.2 \,\mu$ A and it

nearly doubled to  $-25.3 \pm 2.6 \,\mu\text{A}$  for Co-400. This increment slowed down above 400 °C, but the current trajectory continued as the calcination temperature was increased.

To understand the structural change of Co sites with the temperature, we measured the infrared spectra of CoPC-2Py. CoPC-2Py was annealed in a diffuse reflectance infrared Fourier transform spectroscopy (DRIFT) cell under  $N_2$  at a

heating rate of 2 °C per min. The infrared spectra were collected at every 50 °C, as shown in Figure 4d. While the aromatic C-H stretching/bending and the ring breathing mode (1600-1400 cm<sup>-1</sup>) cannot be distinguished between the CoPC and 3-propanol pyridine, we analyzed the change of the level of the O-H (broad peak at 3350 cm<sup>-1</sup>) and sp<sup>3</sup> C-H (sharp peaks at 2930 and 2856 cm<sup>-1</sup>) stretching from 3propanol pyridine. The intensities of both stretching peaks decreased along with the temperature (Figure 4e). There was a sharp decrease at 300 °C. We attributed this change to the thermal removal of the axial ligands of CoPC-2Py, where the axial position of Co became available for catalysis. This temperature correlates well with the ORR activity, as Co catalysts made at 250 °C and below were inactive. We could conclude that fully coordinated octahedral Co sites are not catalytically active in reducing O2. Moreover, the change in the extent of the O-H and sp<sup>3</sup> C-H stretching also shows a continuous decrease with T until ~420 °C, where the axial ligands are likely removed completely. These active Co sites are structurally close to molecular CoPC with sp<sup>2</sup> C-H stretching at 3030 cm<sup>-1</sup> and aromatic C-N stretching at 1321 and 1290 cm<sup>-1</sup>. At 600 °C and above, CoPC-like spectral features disappeared, indicating that phthalocyanine carbonized around 600 °C and square planar Co sites became less symmetric or as SACs (see Figure S8 for details). We note that the further increase of temperature (>600 °C) would increase the graphitization degree of the ligand environments of Co SACs, known to improve the conductivity and activity of SACs.41

ORR kinetics were investigated using rotating disk voltammetry (RDV) in 0.1 M Na<sub>2</sub>SO<sub>4</sub>. Figure 5a exhibits the RVDs of Co-800 at rotation rates of 400-3600 rpm. The diffusion-limited current density increased with the rotation speed of the electrode as a typical characteristic for catalytic reduction of O<sub>2</sub>. The onset potential for the reduction of the  $O_2$  was approximately -0.27 V, close to that measured by CV. These curves were fitted using the Koutecky-Levich (K-L) method by plotting the reciprocal of current density  $(J^{-1})$  as a function of the square root of the rotation rate  $(\omega^{1/2})$ (Figure 5b). The linearity of the fit is considered as a standard firstorder kinetics plot with respect to the concentration of dissolved O2. The number of electrons transferred (n) obtained from the slope was 2.2, 2.0, and 1.9 at -0.4, -0.6, and -0.8 V, respectively. Since the number of electrons transferred was very close to 2 and independent of the potential, this suggests that Co-800 is active in reducing O<sub>2</sub> through two-electron reduction.

The relative yield of  $H_2O_2$  was measured by rotating-ringdisk voltammetry (RRDV). The platinum ring held at a constant potential of 20 mV to oxidize  $H_2O_2$  with a collection efficiency (N) of 22%.  $^{42,43}$  The percentage yield of  $H_2O_2$ 

formation was determined from the currents at the ring and the disk

$$2I_R/N$$
 $H_2O_2(\%) = _____ × 100\%$ 
 $I_D + I_R$ 

where  $I_D$  is the disk current,  $I_R$  is the ring current, and N is the collection efficiency of the ring electrode. The yield of  $H_2O_2$  was ~85% in the potential range of -0.2 to -0.8 V.  $H_2O_2$ , as the major product during the ORR, is in agreement with the average number of electrons transferred of ~2 measured from the K–L method. Additionally, we examined the stability of Co-800 by using constant-potential electrolysis (i-t). Figure 5e shows the i-t curves obtained at -0.4 to -1 V. Generally, the steady state current of Co-800 increased with increasing negative potential. In all cases, the catalysts were stable during electrolysis for 4 h, and no obvious decrease in activity was seen under all potentials. Co-800 as distorted square planar Co sites are strongly anchored on carbon that significantly enhances catalytic durability.

We measured the concentration of  $H_2O_2$  quantitatively as the product in the electrolyte. Using an H-cell that separates the anode and cathode, the amount of  $H_2O_2$  was measured using a colorimetry assay with leucocrystal violet. He oxidation of leucocrystal violet gives absorbance of the product at 596 nm, and it can be calibrated in a standard linear range of known concentrations of  $H_2O_2$  (Figure S9). Figure 6a shows the amount of  $H_2O_2$  produced at -0.4 V (see more potentials in Figure S9). The concentration of  $H_2O_2$  increased linearly with the electrolysis time. The maximum yield of  $H_2O_2$  was 97.4  $\mu$ M after 1 h. The Faradaic efficiency (FE) that defines electron utilization efficiency to specifically produce  $H_2O_2$  was in the range of >80% during the electrolysis for 1 h at -0.4 V. This number was consistent with those measured from RRDV, as shown in Figure 5.

Using RRDVs, we further examined the efficiency of H<sub>2</sub>O<sub>2</sub> production for all of the Co catalysts obtained at different temperatures. Since all Co samples produced below 300 °C were inactive for the reduction of the O2 concentration, their efficiency was negligible. For Co catalysts calcined in the temperature range of 300-450 °C, the selectivity of H<sub>2</sub>O<sub>2</sub> gradually increased from 52.8 to 71.3%. Those values were close to that of molecular CoPC, as reported previously. 27,47,48 Those results suggest that Co catalysts were still in their molecular form supported on carbon, as confirmed by XANES and DRIFT measurements. All catalysts calcined above 600 °C showed very similar H<sub>2</sub>O<sub>2</sub> selectivity of >85%, although their activity was somewhat different. Co-800 has a selectivity of 89.6% at -0.4 V toward H<sub>2</sub>O<sub>2</sub>. By systematically manipulating the active sites and their supporting material using rational engineering approaches,

the exceptional performance of these SACs can be attributed to the synergistic effects of Co single sites and the activated carbon support, which offers a large surface area, enabling facile accessibility to active sites and efficient mass transfer during catalytic reactions. We attribute the high selectivity for  $H_2O_2$  production to the atomically dispersed Co sites. The distorted Co-N<sub>4</sub> sites are likely to be the active centers for two-electron ORRs.  $^{26-29,35,49-51}$ 

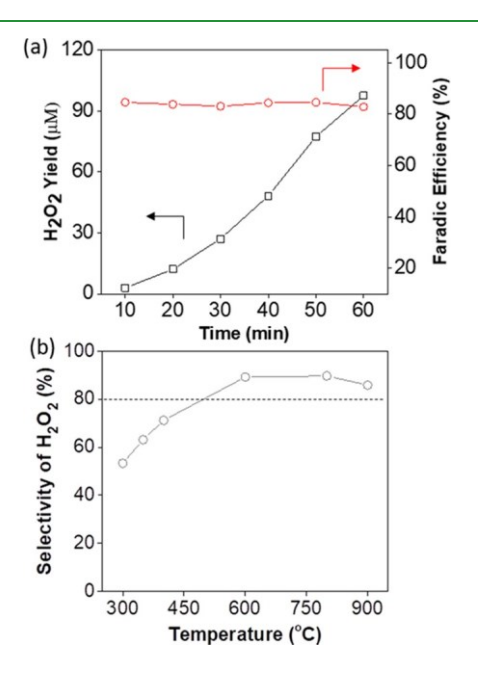


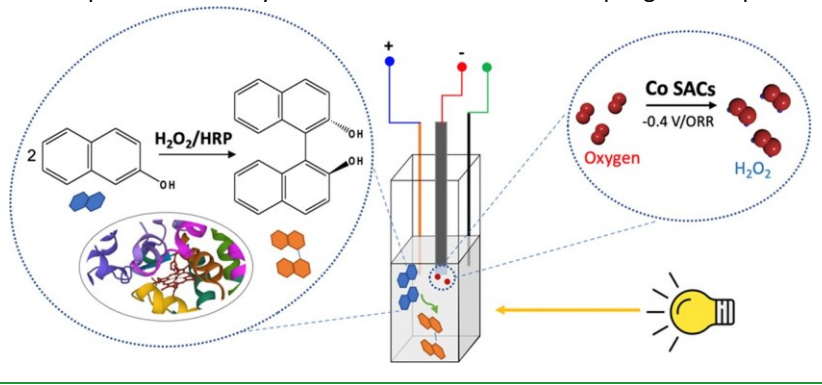
Figure 6. (a)  $H_2O_2$  yield and FE of Co-800 toward  $H_2O_2$  at -0.4 V in  $Na_2SO_4$ . (b) Selectivity of  $H_2O_2$  of Co catalysts calcined at different temperatures. The selectivity was calculated from the RRDV at -0.4 V

opportunities for straightforward applications, e.g., coupled with peroxidases to activate stable C-H bonds (Scheme 2). We examined the oxidative coupling of 2-naphthol to binaphthol catalyzed by HPR and Co SACs. HPR was immobilized and cross-linked on magnetic beads through layer-by-layer assembly with polylysine.<sup>52</sup> The cascade reaction was done in a bicontinuous microemulsion consisting of cetyltrimethylammonium bromide, butanol, hexadecane, and H<sub>2</sub>O (5:5.4:1:88.6, wt %), 53-55 that not only provides solubility for 2-naphthol in the oil phase and water for proper enzyme function but also acts as a supporting electrolyte for the electroreduction of O<sub>2</sub>. Figure 7a shows the constant potential electrolysis in the microemulsion. Co-800 films on the electrodes were very stable in the high solvating microemulsions, where the O<sub>2</sub> reduction currents remained nearly constant with time, similar to those measured in Na<sub>2</sub>SO<sub>4</sub>. The formation of H<sub>2</sub>O<sub>2</sub> was confirmed by using H<sub>2</sub>O<sub>2</sub> testing stripes. After mixing HPR beads and 2naphthol in the microemulsion, the oxidative coupling was done at -0.4 V for 1 h. Using gas chromatography, the

The ORR kinetics of Co-800 were also examined in 0.1 M NaOH at pH 13 (Figure S10). The diffusion-limited current was higher than those obtained at pH 7. While the reduction occurred at much faster kinetics, the yield of  $H_2O_2$  was still >75% in the potential range of -0.3 to -1 V. Co-800 was also very stable under alkaline conditions, as shown by amperometry (Figure S10e). These results clearly illustrate that Co-800 is viable and efficient in catalyzing two-electron ORR and producing  $H_2O_2$  in basic solutions.

Co SACs that reduce  $O_2$  to  $H_2O_2$  selectively provide more formation of binaphthol was confirmed with a well-resolved elution peak at 19.8 min. The conversion of 2-naphthol was estimated to be 80% using 6-bromo-2-naphthol as an internal standard. In negative controls, no product was detected in the absence of HPR or without Co SACs. Therefore, the two catalysts, Co-800 and HRP, worked cooperatively to drive consecutive reactions, i.e.,

Scheme 2. Chemical Structure Equation for Catalytic Production of H<sub>2</sub>O<sub>2</sub> and Coupling of 2-Naphthol



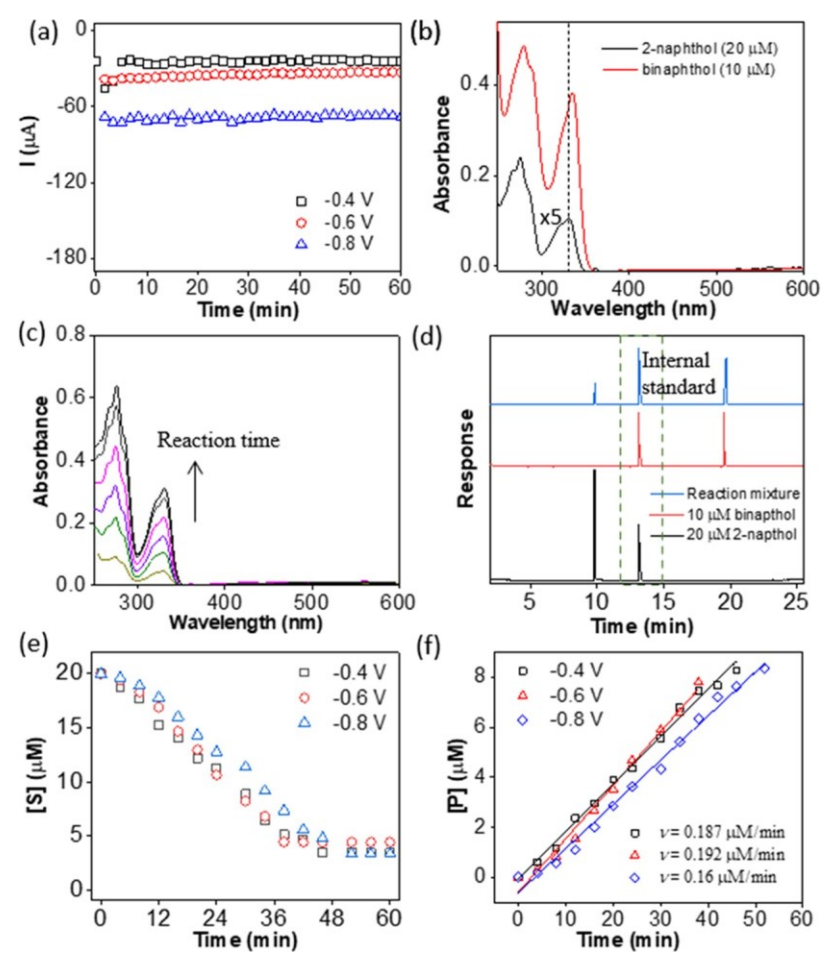


Figure 7. In situ oxidative coupling of 2-naphthol by HRP in combination used with Co-800 in an  $O_2$ -saturated microemulsion of cetyltrimethylammonium bromide, butanol, hexadecane, and  $H_2O$  (5:5.4:1:88.6, wt %). (a) i-t curves of Co-800 for  $H_2O_2$  production at -0.4, -0.6, and -0.8 V in the microemulsion. (b) UV-vis spectra of 2-naphthol and binaphthol. (c) UV-vis kinetics of oxidative coupling of 2-naphthol. The spectra were collected every 10 min. (d) GC elution curves of standard 2-naphthol, binaphthol, 6-bromo-2-naphthol (as the internal standard), and reaction mixture including the internal standard. (e) Concertation of the substrate plotted as a function of reaction time at different potentials. (f) Linear fits of the formation rate of binaphthol at different potentials.

oxidation of  $O_2$  to  $H_2O_2$  by Co-800 and  $H_2O_2$ -activation of HRP to oxidize 2-naphthol by HRP.

In situ oxidative coupling kinetics of 2-naphthol was measured by using UV-vis spectroelectrochemistry. In brief, the three-electrode systems were built in a cuvette. A Pt wire with a diameter of 0.25 mm was used as a counter

electrode, and a Ag wire with a diameter of 0.5 mm was used as a reference electrode. All electrodes were placed outside of the pathway of incident light. The reaction kinetics were monitored by absorption spectra of the solution mixture at different reaction times. Figure 7b shows the UV-vis spectra of 2-naphthol and binaphthol. Their

absorption peaks were fairly close to each other (e.g., 331 nm for 2-naphthol and 334 nm for binaphthol), but the molar absorbability of binaphthol was ~27 times higher than that of 2-naphthol. With the increase of the electrolysis time, there was a fast increase of UV-vis absorbance around 330 nm. Using their molar absorbability, we calculated the conversion of 2-naphthol, as given in Figure 7e, as the change of [S] with reaction time (see details in Figures S11-S12). Interestingly, the consumption rate of 2-naphthol at different potentials nearly overlapped. This agrees well with the formation rate of binaphthol, as plotted in Figure 7f. The formation rate (or the half reactant consumption rate) was in the range of 0.16–0.19  $\mu$ M/min, with small changes at different potentials. These results suggest that the production of H<sub>2</sub>O<sub>2</sub> is unlikely to be the ratedetermining step, but the overall reaction is controlled by the enzymatic dimerization of 2-naphthol by HRP. In other words, the production rate of H<sub>2</sub>O<sub>2</sub> was much faster than its consumption rate by HRP. The turnover frequency, i.e., the transformation of subtracts on each heme center per unit time, was 0.02 s<sup>-1</sup>, close to that of HRP for peroxide activation.56

## 3. CONCLUSIONS

In summary, we demonstrated a robust strategy to catalyze in situ C-H oxidation by combining Co SACs on electrodes and HRP on magnetic beads. Using CoPC-2Py loaded on activated carbon, we investigated the stepwise removal of axial pyridine moieties through thermal annealing to tune the coordination environment of the Co sites. Co-800 showed excellent optimized catalytic performance in producing  $H_2O_2$  at a concentration of 97  $\mu$ M. Co catalysts obtained below 300 °C were inactive due to the retention of the octahedral coordination. Increasing the calcination temperature led to improvement in activity for the ORR, while the molecular Co species formed at below 600 °C were less selective to reduce the level of the O<sub>2</sub> in a two-electron pathway. DRIFT measurements confirmed that the removal of axial ligands occurred above 300 °C, while the aromatic ring frameworks of CoPC disappeared at 600 °C and above, suggesting that phthalocyanine carbonized and Co sites converted to single atoms supported on carbon. These structural features were further confirmed by XANES and correlated with the ORR activity. The FE of Co-800 toward  $H_2O_2$  was 82–85% at –0.4 V, where the distorted Co– $N_4$  sites were likely the active centers for two-electron ORRs. Co SACs were further coupled with HRP to drive the catalytic cascade of the reaction of O2 to H2O2 and the oxidation of 2naphthol in microemulsions. The high selectivity (~100%) and yield (~80%) of binaphthol were confirmed by gas chromatography and spectroelectrochemistry. Our results provide new insights into the design of highly effective,

stable SACs potentially for selective C-H activation when coupled with natural enzymes.

### 4. EXPERIMENTAL SECTION

- **4.1. Materials and Chemicals.** Cobalt phthalocyanine (CoPC, 97%), 3-propanol pyridine (ACS grade, ≥99%), sodium hydroxide (NaOH, bioXtra ≥98%), sodium sulfate (Na<sub>2</sub>SO<sub>4</sub> BioXtra ≥98%), horseradish peroxidase (HRP, MW: 40 kDa), leucocrystal violet (MW: 373.5 g/mol), hydrochloric acid, acetate buffer (pH 4.5), hydrogen peroxide (H<sub>2</sub>O<sub>2</sub>), and Nafion were obtained from SigmaAldrich. Printex U carbon was gifted by the Orion-engineered carbons. All chemicals were used without further purification. HRP was cross-linked using EDC coupling chemistry at each bilayer of (PLL/HRP)<sub>2c</sub> layer-by-layer (LbL) films on 1 mm diameter carboxylated magnetic beads (MB), as described previously. <sup>53,54,56</sup> Assays for HRP-MB activity showed that cross-linked HRP in films on MNPs has similar activity to free HRP. <sup>57</sup>
- **4.2. Synthesis of the CoPC-2Py Complex.** CoPC-2Py was synthesized by adding 3-propanol pyridine and the CoPC complex with a molar ratio of 1:2 (mol) in chloroform. The solution was stirred under  $N_2$  to fully dissolve and disperse CoPC.
- 4.3. Synthesis of Co SACs. Activated carbon was first nitrided through a soft nitriding route, as reported previously. 58-60 4 g of Printex U carbon (4 g) was mixed with 6 g of urea. After grounded together, the mixture was sealed in a crucible with foil and calcined at 150 °C for 2 h and then 300 °C for another 2 h.58,59 The obtained product was washed with water and ethanol several times to remove residual urea and then dried at 50 °C overnight. Co SACs were produced by a pyrolysis method. In a typical synthesis, the concentrated solution of CoPC-2Pv (2 mg) in 5 mL of CHCl<sub>3</sub> was mixed with 200 mg of activated carbon dispersed in CHCl<sub>3</sub> and then stirred overnight. The solvent was then evaporated slowly in a fume hood under a flow of N2. The dried powder was collected and placed on a ceramic crucible tray for thermal treatment in a tube furnace under N2. The temperature was increased at a ramping rate of 5 °C/ min, and the desired temperature was held for 2 h. The sample was cooled down with a decrement rate of 15 °C/min. Using the same protocol, the sample was treated at different temperatures ranging from 100 to 900 °C.
- **4.4. Electrochemical Measurements.** An electrochemical CH 1040 workstation was used for the electrochemical characterization. An SCE was used as a reference electrode, and the graphite rod was used as a counter electrode. The working electrode was made on a pyrolytic graphite rod with the catalyst ink. The ink was prepared by adding 6 mg of catalyst in 1140  $\mu$ L of water, 350  $\mu$ L of isopropanol, and 10  $\mu$ L of 5% Nafion solution. After the solution was sonicated for 25 min, 10  $\mu$ L of the resultant solution was dropped on a pyrolytic graphite rod.

The CVs were measured in 0.1 M Na $_2$ SO $_4$  and 0.1 M NaOH at pH 7 (neutralized with trace NaOH) and 13, respectively. The pH was calibrated with a pH meter. The scan rate was 50 mV/s unless otherwise noted. The electrolyte was saturated with N $_2$  and O $_2$  prior to the test. For RDV and RRDV measurements, pine wave vortex 10 was used as an electrode rotator, and the E7R8 thin gap fixed-disk electrode (ring-disk gap of 180  $\mu$ m) from PINE research was used. For the RRDE measurement, the collection efficiency was calibrated using potassium ferricyanide at a 1600 rpm rotation rate in 0.1 M Na $_2$ SO $_4$  and 0.1 M NaOH at the scan rate of 50 mV/s. The disk electrode was scanned catholically, while the ring

potential was constant at 20 mV. The production of  $H_2O_2$  was also determined using the leucocrystal violet assay. The calibration curve was used with the standard concentrations of  $H_2O_2$  (Figure S9).

**4.5.** In Situ Oxidative Coupling. For in situ conversion of 2naphthol to binaphthol, the reaction system was built in a UV cell. The electrodes were placed in 2 mL of microemulsions without interfering with the pathway of the probe UV light. The kinetics of the reaction were determined using the change of absorbance. The concentration of 2-naphthol and binaphthol was calculated from the UV-vis spectra (see details in Figure S11). The concentration of HRP was  $6.35~\mu g/mL$  in the reaction mixture.

**4.6. Other Characterizations.** Scanning electron microscopy (SEM) and energy dispersive X-ray spectroscopy (EDX) were performed using an FEI Nova NanoSEM 450. The samples were drop-cast onto a silicon wafer and dried at room temperature. The EDX mapping was measured on a large area of the sample at 10 kV, and the exposure to the beam for a long time was avoided to minimize the beam-induced effect, as both activated carbon and cobalt are sensitive to the X-ray beam. HAADF-STEM imaging was recorded on a Titan Themis probe-corrected microscope. The samples were first cleaned by 17 h of beam shower and 15 s of plasma. The UV-vis results were collected on a Cary 60 spectrometer. TGA Q500 was used to analyze the sample annealing from 100 to 700 °C with a rate of heating at 10 °C/min under N<sub>2</sub>. <sup>1</sup>H NMR spectra were recorded on a Bruker Avance 400 MHz spectrometer. X-ray absorption spectroscopy (XAS) measurements at the Co K-edge (7709 eV) were performed at the 7-BM (QAS) beamline of National Synchrotron Light Source II (NSLS II), Brookhaven National Laboratory. The CoPc sample was mixed and ground with boron nitride, prepared as a pellet and measured in the transmission mode. Other samples were prepared as pellets and measured in fluorescence mode. The infrared spectra at different temperatures were analyzed on a Thermo Nicolet NEXUS 670 with a DRIFT cell. The fluorescence spectra of CoPC2Py were recorded on a Cary Eclipse fluorescence spectrophotometer.



# ASSOCIATED CONTENT

## \* Supporting Information

The Supporting Information is available free of charge at https://pubs.acs.org/doi/10.1021/acsami.3c03053.

Further characterization of CoPC complexes and SACs, electrochemical analysis, and kinetic data on HRP catalysis (PDF)



# **AUTHOR INFORMATION**

## **Corresponding Authors**

James F. Rusling – Department of Chemistry, University of

Connecticut, Storrs, Connecticut 06269, United States; Institute of Materials Science, University of Connecticut,

Storrs, Connecticut 06269, United States; Department of

Surgery and Neag Cancer Center, Uconn Health, Farmington, Connecticut 06030, United States; School of

Chemistry, National University of Ireland at Galway, Galway

H91 TK33, Ireland; o orcid.org/0000-0002-6117-3306; Email: james.rusling@uconn.edu

Anatoly I. Frenkel – Department of Materials Science and

Chemical Engineering, Stony Brook University, Stony Brook, New York 11790, United States; Division of Chemistry,

Brookhaven National Laboratory, Upton, New York 119735000, United States; o orcid.org/0000-0002-5451-1207;

Email: anatoly.frenkel@stonybrook.edu

Jie He – Department of Chemistry, University of Connecticut,

Storrs, Connecticut 06269, United States; Institute of Materials Science, University of Connecticut, Storrs, Connecticut 06269, United States; orcid.org/0000-0003-

0252-3094; Email: jie.he@uconn.edu

### **Authors**

Maham Liaqat – Department of Chemistry, University of Connecticut, Storrs, Connecticut 06269, United States
Rumasha Nipuni Thiruwana Kankanamage – Department of

Chemistry, University of Connecticut, Storrs, Connecticut

*06269, United States;* orcid.org/0000-0002-3873-2499

Hanyi Duan – Department of Chemistry, University of Connecticut, Storrs, Connecticut 06269, United States;
orcid.org/0000-0001-8720-2761

Ryuichi Shimogawa – Department of Materials Science

Chemical Engineering, Stony Brook University, Stony Brook.

New York 11790, United States

Jiyu Sun – Institute of Materials Science, University of Connecticut, Storrs, Connecticut 06269, United States;

orcid.org/0000-0001-5223-7075

Monia Nielsen – Department of Materials Science and Engineering, University of Connecticut, Storrs, Connecticut 06269, United States Ehab Shaaban – Department of Chemistry, University of New

Hampshire, Durham, New Hampshire 03824, United States

Yuanyuan Zhu – Department of Materials Science and Engineering and Institute of Materials Science, University of

Connecticut, Storrs, Connecticut 06269, United States;
o orcid.org/0000-0002-5257-5645

Puxian Gao – Department of Materials Science and Engineering and Institute of Materials Science,

Connecticut, Storrs, Connecticut 06269, United States;

orcid.org/0000-0002-2132-4392

Complete contact information is available at: https://pubs.acs.org/10.1021/acsami.3c03053

### **Author Contributions**

University of

J.H., M.L., and J.R. conceived the idea and co-wrote the first draft, M.L. carried out the synthesis of materials and electrochemical characterizations, R.N.T.K. worked on enzyme immobilization and catalysis, H.D. conducted the characterization of CoPC complexes, R.S., E.S., and A.I.F. conducted the XAS characterizations and calculations, J.S. and P.G. carried out the DRIFT measurement, and M.N. and Y.Z. did STEM characterizations. All authors discussed the results and commented on the manuscript.

#### **Notes**

The authors declare no competing financial interest.



## **ACKNOWLEDGMENTS**

J.H. and J.R. are grateful for the support from the National Science Foundation (CBET-2035669) and the University of Connecticut through the research excellence program. The TEM studies were performed using the facilities in the UConn/Thermo Fisher Scientific Center for Advanced Microscopy and Materials Analysis (CAMMA). A.I.F. acknowledges support of this work by the US National Science Foundation under Award 2102299. This research used beamline 7-BM (QAS) of the National Synchrotron Light Source II, a U.S. DOE Office of Science User Facility operated for the DOE Office of Science by the Brookhaven National Laboratory under Contract No. DE-SC0012704. Beamline operations were supported in part by the Synchrotron Catalysis Consortium (U.S. DOE, Office of Basic Energy Sciences, Grant No. DE-SC0012335). The authors thank Drs. Lu Ma, Steven Ehrlich, Prahlad Routh, and Nebojsa Marinkovic for their help with the beamline measurements at the QAS beamline.



### **REFERENCES**

- (1) Sies, H.; Belousov, V. V.; Chandel, N. S.; Davies, M. J.; Jones, D. P.; Mann, G. E.; Murphy, M. P.; Yamamoto, M.; Winterbourn, C. Defining Roles of Specific Reactive Oxygen Species (ROS) in Cell Biology and Physiology. *Nat. Rev. Mol. Cell Biol.* 2022, 23 (7), 499–515.
- (2) Ahmad, T.; Iqbal, A.; Halim, S. A.; Uddin, J.; Khan, A.; El Deeb, S.; Al-Harrasi, A. Recent Advances in Electrochemical Eensing of Hydrogen Peroxide (H2O2) Released from Cancer Cells. *Nanomaterials* 2022, *12* (9), 1475.
- (3) Xing, L.; Zhang, W.; Fu, L.; Lorenzo, J. M.; Hao, Y. Fabrication and Application of Electrochemical Sensor for Analyzing Hydrogen Peroxide in Food System and Biological Samples. *Food Chem.* 2022, *385*, No. 132555.
- (4) Liu, B.; Wang, P.; Lopes, A.; Jin, L.; Zhong, W.; Pei, Y.; Suib, S. L.; He, J. Au–Carbon Electronic Interaction Mediated Selective Oxidation of Styrene. *ACS Catal.* 2017, *7* (5), 3483–3488.
- (5) Matsunaga, I.; Shiro, Y. Peroxide-Utilizing Biocatalysts: Structural and Functional Diversity of Heme-Containing Enzymes. *Curr. Opin. Chem. Biol.* 2004, *8* (2), 127–132.
- (6) Hernandez, K.; Berenguer-Murcia, A.; C Rodrigues, R.; Fernandez-Lafuente, R. Hydrogen Peroxide in Biocatalysis. A Dangerous Liaison. *Curr. Org. Chem.* 2012, *16* (22), 2652–2672.
- (7) Sigmund, M.-C.; Poelarends, G. J. Current State and Future Perspectives of Engineered and Artificial Peroxygenases for the Oxyfunctionalization of Organic Molecules. *Nat. Catal.* 2020, *3* (9), 690–702.
- (8) Wang, X.; Yao, B.; Su, X. Linking Enzymatic Oxidative Degradation of Lignin to Organics Detoxification. *Int. J. Mol. Sci.* 2018, *19* (11), 3373.
- (9) Huang, Y.; Lin, J.; Zou, J.; Xu, J.; Wang, M.; Cai, H.; Yuan, B.; Ma, J. ABTS as an Electron Shuttle to Accelerate the Degradation of Diclofenac with Horseradish Peroxidase-Catalyzed Hydrogen Peroxide Oxidation. *Sci. Total Environ.* 2021, *798*, No. 149276.
- (10) Lewis, R. J.; Koy, M.; Macino, M.; Das, M.; Carter, J. H.; Morgan, D. J.; Davies, T. E.; Ernst, J. B.; Freakley, S. J.; Glorius, F.; Hutchings, G. J. N-Heterocyclic Carbene Modified Palladium Catalysts for the Direct Synthesis of Hydrogen Peroxide. *J. Am. Chem. Soc.* 2022, *144* (34), 15431–15436.
- (11) Chen, J.; Ma, Q.; Zheng, X.; Fang, Y.; Wang, J.; Dong, S. Kinetically Restrained Oxygen Reduction to Hydrogen Peroxide with Nearly 100% Selectivity. *Nat. Commun.* 2022, *13* (1), No. 2808.
- (12) Dan, M.; Zhong, R.; Hu, S.; Wu, H.; Zhou, Y.; Liu, Z.-Q. Strategies and Challenges on Selective Electrochemical Hydrogen Peroxide Production: Catalyst and Reaction Medium Design. *Chem. Catal.* 2022, *2* (8), 1919–1960.
- (13) Jin, L.; Thanneeru, S.; Cintron, D.; He, J. Bioinspired Design of Hybrid Polymer Catalysts with Multicopper Sites for Oxygen Reduction. *ChemCatChem* 2020, *12* (23), 5932–5937.
- (14) Thanneeru, S.; Milazzo, N.; Lopes, A.; Wei, Z.; Angeles-Boza, A. M.; He, J. Synthetic Polymers to Promote Cooperative Cu Activity for O<sub>2</sub> Aactivation: Poly vs Mono. *J. Am. Chem. Soc.* 2019, 141 (10), 4252–4256.
- (15) Siahrostami, S.; Verdaguer-Casadevall, A.; Karamad, M.; Deiana, D.; Malacrida, P.; Wickman, B.; Escudero-Escribano, M.;

- Paoli, E. A.; Frydendal, R.; Hansen, T. W. Enabling Eirect H2O2 Production through Rational Electrocatalyst Design. *Nat. Mater.* 2013, *12* (12), 1137–1143.
- (16) Verdaguer-Casadevall, A.; Deiana, D.; Karamad, M.; Siahrostami, S.; Malacrida, P.; Hansen, T. W.; Rossmeisl, J.; Chorkendorff, I.; Stephens, I. E. Trends in the Electrochemical Synthesis of H2O2: Enhancing Activity and Selectivity by Electrocatalytic Site Engineering. *Nano Lett.* 2014, *14* (3), 1603–1608.
- (17) Zou, Y.; Guo, X.; Bian, X.; Zhang, Y.; Lin, W.; Huang, S.; Chen, Z.; Ding, K. Tailoring 2-Electron Oxygen Reduction Reaction Selectivity on h-BN-based Single-Atom Catalysts from Superoxide Dismutase: A DFT Investigation. *Appl. Surf. Sci.* 2022, *592*, No. 153233.
- (18) Nallayagari, A. R.; Sgreccia, E.; Pasquini, L.; Sette, M.; Knauth, P.; Di Vona, M. L. Impact of Anion Exchange Ionomers on the Electrocatalytic Performance for the Oxygen Reduction Reaction of BN Co-doped Carbon Quantum Dots on Activated Carbon. ACS Appl. Mater. Interfaces 2022, 14 (41), 46537–46547.
- (19) Wei, G.; Liu, X.; Zhao, Z.; Men, C.; Ding, Y.; Gao, S. Constructing Ultrahigh-Loading Unsymmetrically Coordinated ZnN3O Single-Atom Sites with Efficient Oxygen Reduction for H2O2 Production. *Chem. Eng. J.* 2023, 455, No. 140721.
- (20) Yang, X.; Zeng, Y.; Alnoush, W.; Hou, Y.; Higgins, D.; Wu, G. Tuning Two-eElectron Oxygen-Reduction Pathways for H2O2 Electrosynthesis via Engineering Atomically Dispersed Single Metal Site Catalysts. *Adv. Mater.* 2022, *34* (23), No. 2107954.
- (21) Han, A.; Wang, X.; Tang, K.; Zhang, Z.; Ye, C.; Kong, K.; Hu, H.; Zheng, L.; Jiang, P.; Zhao, C.; et al. An Adjacent Atomic Platinum Site Enables Single-Atom Iron with High Oxygen Reduction Reaction Performance. *Angew. Chem., Int. Ed.* 2021, *60* (35), 19262–19271.
- (22) Kattel, S.; Wang, G. A Density Functional Theory Study of Oxygen Reduction Reaction on Me–N<sub>4</sub> (Me= Fe, Co, or Ni) Clusters between Graphitic Pores. *J. Mater. Chem. A* 2013, *1* (36), 10790–10797.
- (23) Cai, Z.; Du, P.; Liang, W.; Zhang, H.; Wu, P.; Cai, C.; Yan, Z. Single-Atom-Sized Ni–N<sub>4</sub> Sites Anchored in Three-Dimensional Hierarchical Carbon Nanostructures for the Oxygen Reduction Reaction. *J. Mater. Chem. A* 2020, *8* (30), 15012–15022.
- (24) Zhang, J.; Yang, H.; Liu, B. Coordination Engineering of SingleAtom Catalysts for the Oxygen Reduction Reaction: a review. *Adv. Energy Mater.* 2021, *11* (3), No. 2002473.
- (25) Yin, P.; Yao, T.; Wu, Y.; Zheng, L.; Lin, Y.; Liu, W.; Ju, H.; Zhu, J.; Hong, X.; Deng, Z.; et al. Single Cobalt Atoms with Precise NCoordination as Superior Oxygen Reduction Reaction Catalysts. *Angew. Chem.* 2016, *128* (36), 10958–10963.
- (26) Feng, Y.-C.; Wang, X.; Yi, Z.-Y.; Wang, Y.-Q.; Yan, H.-J.; Wang, D. In-situ ECSTM Investigation of  $H_2O_2$  Production in Cobalt Porphyrin-Catalyzed Oxygen Reduction Reaction. *Sci. China Chem.* 2022, *66*, 273–278.
- (27) Zhao, Q.; Wang, Y.; Lai, W.-H.; Xiao, F.; Lyu, Y.; Liao, C.; Shao, M. Approaching a High-Rate and Sustainable Production of Hydrogen Peroxide: Oxygen Reduction on Co-N-C Single-Atom Electrocatalysts in Simulated Seawater. *Energy Environ. Sci.* 2021, 14 (10), 5444–5456.
- (28) Xu, H.; Zhang, S.; Geng, J.; Wang, G.; Zhang, H. Cobalt Single Atom Catalysts for the Efficient Electrosynthesis of Hydrogen Peroxide. *Inorg. Chem. Front.* 2021, *8* (11), 2829–2834.

- (29) Jung, E.; Shin, H.; Lee, B.-H.; Efremov, V.; Lee, S.; Lee, H. S.; Kim, J.; Hooch Antink, W.; Park, S.; Lee, K.-S.; et al. Atomic-Level Tuning of Co–N–C Catalyst for High-Performance Electrochemical H<sub>2</sub>O<sub>2</sub> Production. *Nat. Mater.* 2020, *19* (4), 436–442.
- (30) Huang, P.; Huang, J.; Li, J.; Pham, T. D.; Zhang, L.; He, J.; Brudvig, G. W.; Deskins, N. A.; Frenkel, A. I.; Li, G. Revealing the Structure of Single Cobalt Sites in Carbon Nitride for Photocatalytic CO<sub>2</sub> Reduction. *J. Phys. Chem. C* 2022, *126* (20), 8596–8604.
- (31) Xiang, S.; Huang, P.; Li, J.; Liu, Y.; Marcella, N.; Routh, P. K.; Li, G.; Frenkel, A. I. Solving the Structure of "Single-Atom" Catalysts using Machine Learning Assisted XANES Analysis. *Phys. Chem. Chem. Phys.* 2022, *24* (8), 5116–5124.
- (32) Huang, P.; Huang, J.; Pantovich, S. A.; Carl, A. D.; Fenton, T. G.; Caputo, C. A.; Grimm, R. L.; Frenkel, A. I.; Li, G. Selective CO<sub>2</sub> Reduction Catalyzed by Single Cobalt Sites on Carbon Nitride under Visible-Light Irradiation. *J. Am. Chem. Soc.* 2018, *140* (47), 16042–16047.
- (33) Ghani, F.; Kristen, J.; Riegler, H. Solubility Properties of Unsubstituted Metal Phthalocyanines in Different Types of Solvents. *J. Chem. Eng. Data* 2012, *57* (2), 439–449.
- (34) Wu, Y.; Liang, Y.; Wang, H. Heterogeneous Molecular Catalysts of Metal Phthalocyanines for Electrochemical CO<sub>2</sub> Reduction Reactions. *Acc. Chem. Res.* 2021, *54* (16), 3149–3159.
- (35) Wu, J.; Mehmood, A.; Zhang, G.; Wu, S.; Ali, G.; Kucernak, A. Highly Selective O<sub>2</sub> reduction to H<sub>2</sub>O<sub>2</sub> Catalyzed by Cobalt Nanoparticles Supported on Nitrogen-Doped Carbon in Alkaline Solution. *ACS Catal.* 2021, *11* (9), 5035–5046.
- (36) Tasso, T. T.; Furuyama, T.; Kobayashi, N. Absorption and Electrochemical Properties of Cobalt and Iron Phthalocyanines and their Quaternized Derivatives: Aggregation Equilibrium and Oxygen Reduction Electrocatalysis. *Inorg. Chem.* 2013, *52* (16), 9206–9215.
- (37) AGirtaŞ, M. S.; Solğun, D. G.; Yildiko, U.; Ozkartal, A. Design of Novel Substituted Phthalocyanines; Synthesis and Dluorescence, DFT, Photovoltaic Properties. *Turk. J. Chem.* 2020, 44 (6), 1574–1586.
- (38) Cao, H.; Gong, M.; Wang, M.; Tang, Q.; Wang, L.; Zheng, X. Steady/Transient State Spectral Researches on the Solvent-Triggered and Photo-Induced Novel Properties of Metal-Coordinated Phthalocyanines. *RSC Adv.* 2022, *12* (10), 5964–5970.
- (39) Kumar, G.; Nampoori, V.; Vallabhan, C.; Jose, G.; Unnikrishnan, N. Emission Spectral Studies of Phthalocyanines in Borate Glass Matrix. *J. Mater. Sci.* 2000, *19*, 1669–1672.
- (40) Liu, Y.; Deb, A.; Leung, K. Y.; Nie, W.; Dean, W. S.; PennerHahn, J. E.; McCrory, C. C. L. Determining the Coordination Environment and Electronic Structure of Polymer-Encapsulated Cobalt Phthalocyanine under Electrocatalytic CO<sub>2</sub> Reduction Conditions using in situ X-Ray Absorption Spectroscopy. *Dalton Trans.* 2020, 49 (45), 16329–16339.
- (41) Xiong, W.; Li, H.; Wang, H.; Yi, J.; You, H.; Zhang, S.; Hou, Y.; Cao, M.; Zhang, T.; Cao, R. Hollow Mesoporous Carbon Sphere Loaded Ni–N<sub>4</sub> Single-Atom: Support Structure Study for CO<sub>2</sub> Electrocatalytic Reduction Catalyst. *Small* 2020, *16* (41), No. 2003943.
- (42) Zhang, J.; Pietro, W. J.; Lever, A. Rotating Ring-Disk Electrode Analysis of  $CO_2$  Reduction Electrocatalyzed by a Cobalt Tetramethylpyridoporphyrazine on the Disk and Detected as CO on a Platinum Ring. *J. Electroanal. Chem.* 1996, 403 (1–2), 93–100.

- (43) Paulus, U.; Schmidt, T.; Gasteiger, H.; Behm, R. Oxygen Reduction on a High-Surface Area Pt/Vulcan Carbon Catalyst: a Thin-Film Rotating Ring-Disk Dlectrode Study. *J. Electroanal. Chem.* 2001, 495 (2), 134–145.
- (44) Zhang, L.-S.; Wong, G. T. Spectrophotometric Setermination of  $H_2O_2$  in Marine Waters with Leuco Crystal Violet. *Talanta* 1994, 41 (12), 2137–2145.
- (45) Mottola, H. A.; Simpson, B. E.; Gorin, G. Absorptiometric Determination of Hydrogen Peroxide in Submicrogram Amounts with Leuco Crystal Violet and Peroxidase as Catalyst. *Anal. Chem.* 1970, 42 (3), 410–411.
- (46) da Silva, L.; Cintra, L. T. A.; de Oliveira Gallinari, M.; de Alcantara, S.; Dos Santos, P.; Chaves Neto, A. H.; Briso, A. L. F. Influence of Different Dye Substances on the Effectiveness of Bleaching and H<sub>2</sub>O<sub>2</sub> Diffusion. *Oper. Dent.* 2022, *47* (6), 648–657.
- (47) Barros, W. R.; Reis, R. M.; Rocha, R. S.; Lanza, M. R. Electrogeneration of Hydrogen Peroxide in Acidic Medium using Gas Diffusion Electrodes Modified with Cobalt (II) Phthalocyanine. *Electrochim. Acta* 2013, *104*, 12–18.
- (48) Hosu, I. S.; Wang, Q.; Vasilescu, A.; Peteu, S. F.; Raditoiu, V.; Railian, S.; Zaitsev, V.; Turcheniuk, K.; Wang, Q.; Li, M.; et al. Cobalt Phthalocyanine Tetracarboxylic Acid Modified Reduced Graphene Oxide: a Sensitive Matrix for the Electrocatalytic Detection of Peroxynitrite and Hydrogen Peroxide. *RSC Adv.* 2015, 5 (2), 1474–1484.
- (49) Gao, J.; bin Yang, H.; Huang, X.; Hung, S.-F.; Cai, W.; Jia, C.; Miao, S.; Chen, H. M.; Yang, X.; Huang, Y.; et al. Enabling Direct  $H_2O_2$  Production in Acidic Media through Rational Design of Transition Metal Single Atom Catalyst. *Chem* 2020, *6* (3), 658–674.
- (50) Ding, J.; Huang, J.; Zhang, Q.; Wei, Z.; He, Q.; Chen, Z.; Liu, Y.; Su, X.; Zhai, Y. A Hierarchical Monolithic Cobalt-Single-Atom Electrode for Efficient Hydrogen Peroxide Production in Acid. *Catal. Sci. Technol.* 2022, *12* (8), 2416–2419.
- (51) Liu, W.; Zhang, C.; Zhang, J.; Huang, X.; Song, M.; Li, J.; He, F.; Yang, H.; Zhang, J.; Wang, D. Tuning the Atomic Configuration of Co-NC Electrocatalyst Enables Highly-Selective  $H_2O_2$  Production in Acidic Media. *Appl. Catal., B* 2022, *310*, No. 121312.
- (52) Otieno, B.; Krause, C.; Rusling, J. Bioconjugation of Antibodies and Enzyme Labels onto Magnetic Beads. In *Methods in Enzymology*; Elsevier, 2016; Vol. *571*, pp 135–150.
- (53) Vaze, A.; Parizo, M.; Rusling, J. F. Enhanced Rates of Electrolytic Styrene Epoxidation Catalyzed by Cross-linked Myoglobin-poly (L-lysine) Films in Bicontinuous Microemulsions. *Langmuir* 2004, *20* (25), 10943–10948.
- (54) Guto, P. M.; Kumar, C. V.; Rusling, J. F. Thermostable Biocatalytic Films of Enzymes and Polylysine on Electrodes and Nanoparticles in Microemulsions. *Langmuir* 2008, *24* (18), 10365–10370.
- (55) Guto, P. M.; Kumar, C. V.; Rusling, J. F. Thermostable Peroxidase– Polylysine Films for Biocatalysis at 90° C. *J. Phys. Chem. B* 2007, *111* (30), 9125–9131.
- (56) Chalkias, N. G.; Kahawong, P.; Giannelis, E. P. Activity Increase of Horseradish Peroxidase in the Presence of Magnetic Particles. *J. Am. Chem. Soc.* 2008, *130* (10), 2910–2911.
- (57) Kankanamage, R. N. T.; Ahiadu, B. K.; He, J.; He, J.; Rusling, J. F. Biocatalytic Nitration of Phenols in Microemulsions at Elevated Temperatures using Enzymes Stabilized on Magnetic Beads. *ChemCatChem* 2023, No. e202300119, DOI: 10.1002/cctc.202300119.

- (58) Zhang, L.; Wei, Z.; Thanneeru, S.; Meng, M.; Kruzyk, M.; Ung, G.; Liu, B.; He, J. A Polymer Solution to Prevent Nanoclustering and Improve the Selectivity of Metal Nanoparticles for Electrocatalytic CO<sub>2</sub> Reduction. *Angew. Chem.* 2019, *131* (44), 15981–15987.
- (59) Jin, L.; Liu, B.; Louis, M. E.; Li, G.; He, J. Highly Crystalline Mesoporous Titania Loaded with Monodispersed Gold Nanoparticles: Controllable Metal–Support Interaction in Porous Materials. *ACS Appl. Mater. Interfaces* 2020, *12* (8), 9617–9627.
- (60) Jin, L.; Liu, B.; Wang, P.; Yao, H.; Achola, L. A.; Kerns, P.; Lopes, A.; Yang, Y.; Ho, J.; Moewes, A.; et al. Ultrasmall Au Nanocatalysts Supported on Nitrided Carbon for Electrocatalytic CO<sub>2</sub> Reduction: the Role of the Carbon Support in High Selectivity. *Nanoscale* 2018, *10* (30), 14678–14686.